AGU PUBLICATIONS

JGR

Journal of Geophysical Research: Space Physics

RESEARCH ARTICLE
10.1002/2017JA024217

Key Points:
- Locations of boundaries (the IMB, the ICB, and the β^*) at Mars show a north-south asymmetry mainly on the nightside
- IMBs coincide with ICBs on the dayside, and all boundaries depend on the SW dynamic pressure and the southern crustal *B* fields
- IMBs and ICBs tend to be located at high altitudes in the nightside, southern, and downward E_{SW} hemisphere

Correspondence to:
K. Seki,
k.seki@eps.s.u-tokyo.ac.jp

Citation:
Matsunaga, K., Seki, K., Brain, D. A., Hara, T., Masunaga, K., Mcfadden, J. P., … Jakosky, B. M. (2017). Statistical study of relations between the induced magnetosphere, ion composition, and pressure balance boundaries around Mars based on MAVEN observations. *Journal of Geophysical Research: Space Physics*, *122*, 9723–9737. https://doi.org/10.1002/2017JA024217

Received 5 APR 2017
Accepted 25 AUG 2017
Accepted article online 30 AUG 2017
Published online 29 SEP 2017

©2017. American Geophysical Union. All Rights Reserved.

Statistical Study of Relations Between the Induced Magnetosphere, Ion Composition, and Pressure Balance Boundaries Around Mars Based On MAVEN Observations

Kazunari Matsunaga[1,2], Kanako Seki[2], David A. Brain[3], Takuya Hara[4], Kei Masunaga[5], James P. Mcfadden[4], Jasper S. Halekas[6], David L. Mitchell[4], Christian Mazelle[7], J. R. Espley[8], Jacob Gruesbeck[9,10], and Bruce M. Jakosky[3]

[1]Institute for Space-Earth Environmental Research, Nagoya University, Nagoya, Japan, [2]Department of Earth and Planetary Science, University of Tokyo, Tokyo, Japan, [3]Laboratory for Atmospheric and Space Physics, University of Colorado Boulder, Boulder, CO, USA, [4]Space Sciences Laboratory, University of California, Berkeley, CA, USA, [5]Swedish Institute of Space Physics, Kiruna, Sweden, [6]Department of Physics and Astronomy, University of Iowa, Iowa City, IA, USA, [7]IRAP, University of Toulouse, CNRS, UPS, CNES, Toulouse, France, [8]NASA Goddard Space Flight Center, Greenbelt, MD, USA, [9]Department of Astronomy, University of Maryland, College Park, MD, USA, [10]Solar System Exploration Division, NASA Goddard Space Flight Center, Greenbelt, MD, USA

Abstract Direct interaction between the solar wind (SW) and the Martian upper atmosphere forms a characteristic region, called the induced magnetosphere between the magnetosheath and the ionosphere. Since the SW deceleration due to increasing mass loading by heavy ions plays an important role in the induced magnetosphere formation, the ion composition is also expected to change around the induced magnetosphere boundary (IMB). Here we report on relations of the IMB, the ion composition boundary (ICB), and the pressure balance boundary based on a statistical analysis of about 8 months of simultaneous ion, electron, and magnetic field observations by Mars Atmosphere and Volatile EvolutioN (MAVEN) mission. We chose the period when MAVEN observed the SW directly near its apoapsis to investigate their dependence on SW parameters. Results show that IMBs almost coincide with ICBs on the dayside and locations of all three boundaries are affected by the SW dynamic pressure. A remarkable feature is that all boundaries tend to locate at higher altitudes in the southern hemisphere than in the northern hemisphere on the nightside. This clear geographical asymmetry is permanently seen regardless of locations of the strong crustal *B* fields in the southern hemisphere, while the boundary locations become higher when the crustal *B* fields locate on the dayside. On the nightside, IMBs usually locate at higher altitude than ICBs. However, ICBs are likely to be located above IMBs in the nightside, southern, and downward E_{SW} hemisphere when the strong crustal *B* fields locate on the dayside.

1. Introduction

Mars does not possess an intrinsic global magnetic field (e.g., Acuña et al., 1998). The solar wind can directly interact with the Martian upper atmosphere and energy, momentum, and material exchanges occur (e.g., Lundin et al., 2011). The direct interactions between the solar wind and the Martian upper atmosphere form a characteristic transitional region between the shocked solar wind (magnetosheath) and the Martian ionosphere. In situ spacecraft observations over the past several decades have led to the identification of several plasma boundaries in the transition region (Nagy et al., 1990): the induced magnetosphere boundary (IMB) (e.g., Vignes et al., 2000; Dubinin et al., 2006), the magnetic pileup boundary (MPB) (e.g., Trotignon et al., 1996, 2006; Matsunaga et al., 2015), the ion composition boundary (ICB) (e.g., Sauer et al., 1994), the planetopause (Riedler et al., 1989), the protonopause (Sauer et al., 1994), the ionopause (e.g., Mitchell et al., 2001), and the pressure balance boundary (e.g., Brain et al., 2010; Xu et al., 2016). The IMB is regarded being as the same as MPB (Vignes et al., 2000), and the ICB is regarded as being the same as protonopause and planetopause (e.g., Breus et al., 1991). Therefore, we will use the following boundary names in this study as being representative of each category of the boundaries: IMB, ICB, and the pressure balance boundary based on β^* (β^* is defined as the ratio of the sum of plasma thermal and dynamic pressure to the magnetic pressure).

Heavy ions generated by photoionization and charges exchange from the Martian neutral atmosphere are accelerated by the solar wind convection electric field. The planetary heavy ions are accelerated by the solar wind convection electric field and exhibit $\boldsymbol{E} \times \boldsymbol{B}$ drift whose guiding center moves with the local solar wind or magnetosheath flows. We call this process the ion pickup. When the density of the pickup heavy ions increases in the solar wind or magnetosheath, the reactions of the ambient flow plasma and magnetic fields are no longer negligible, and conservation of the momentum causes a decrease in velocity. This process is called the mass loading process. The mass loading process forms a transition region where the ion composition changes from solar wind proton dominant regions to planetary heavy ion dominant regions, coinciding with the magnetic field "pileup" due to the velocity decrease (e.g., Breus et al., 1989; Dubinin & Lundin 1995).

When the spacecraft passes the IMB from the magnetosheath to the Martian induced magnetosphere, fluctuations of the magnetic fields and the electron fluxes are known to decrease (e.g., Nagy et al., 2004; Trotignon et al., 2006; Matsunaga et al., 2015). On the other hand, when the spacecraft passes the ICB from the magnetosheath side to the Martian side, the main ion component changes from solar wind protons to planetary heavy ions (e.g., Breus et al., 1991). Previous simulation studies (e.g., Brain et al., 2010) noted that the magnetic pressure, the dynamic pressure, and the thermal pressure contribute to the pressure balance in the plasma environment around Mars. Brain et al. (2010) reported a transition from an upstream region dominated by plasma dynamic pressures, to a magnetosheath region dominated by thermal pressures, to a low altitude region dominated by magnetic pressures. However, recently, Xu et al. (2016) reported that dynamic pressure is important in the flanks of Mars and showed that the β^* boundary, which is determined by the pressure ratio $\beta^* = 1$, coincide reasonably well with the ICB.

A classical view of the induced magnetosphere formation is due to the mass loading process by the planetary heavy ions. In this theory, the IMB and the ICB are expected to be observed at similar locations, at least on the dayside. A sudden increase in the magnitude of the magnetic field at the IMB also appears due to the deflection and piles up the interplanetary magnetic field (IMF) (e.g., Breus et al., 1989; Dubinin & Lundin 1995). The magnetosheath can penetrate to an approximately 400 km altitude (e.g., Brain et al., 2005; Matsunaga et al., 2015). The Kelvin-Helmholtz instability caused by velocity shear across a boundary is also considered to be a possible physical mechanism to characterize the Martian plasma boundary location (e.g., Gurnett et al., 2010; Matsunaga et al., 2015; Ruhunusiri et al., 2016).

Since Mars Global Surveyor (MGS) did not possess an ion detector and its mapping orbit was fixed around at an approximately 400 km altitude (Albee et al., 2001), the ICB and the pressure balance boundary were not able to be investigated by this mission. Both Phobos-2 and Mars Express (MEX) carried an ion mass analyzer, and observed the ICB (e.g., Breus et al., 1991; Dubinin et al., 2006). Unfortunately, the observation period of Phobos-2 was short until its signal was lost while MEX lacked a magnetometer. Thus, the relationship between the IMB, ICB, and pressure balance boundary are still not completely understood due to the lack of long-term simultaneous observations of the magnetic field, electrons, and ion compositions near Mars. Some MHD, multifluid MHD, and hybrid simulations have been developed to investigate the Martian plasma environment, including the plasma balance boundaries (e.g., Brain et al., 2010 and references therein). Utilizing simultaneous ion, electron, and magnetic field observations from the Mars Atmosphere and Volatile EvolutioN (MAVEN) mission, we conducted a statistical study of the IMB, ICB, and pressure balance boundary crossings to investigate their relations and dependences on solar wind conditions and geographical configurations (i.e., the location of strong crustal magnetic fields). The pressure balance boundary is based on the β^* value proposed by Xu et al. (2016) ($\beta^* = (P_{\mathrm{th}} + P_{\mathrm{dyn}})/P_B$, where P_{th}, P_{dyn}, and P_B represent the plasma thermal pressure, the dynamic pressure, and the magnetic pressure, respectively). Hereafter, this boundary is referred to as the "β^* boundary."

In section 2, we introduce the instruments on board MAVEN and the data set used in this study. In section 3, we explain an algorithm to automatically identify the Martian plasma boundaries and show two example events. In section 4, we report on the results of the statistical analyses. Finally, we summarize the results and discuss the global structure of the Martian plasma boundaries in section 5.

2. Instrumentation and Data Set

The MAVEN spacecraft was launched in November 2013 and inserted into orbit around Mars in September 2014 in order to investigate the interactions between the solar wind and the Martian upper atmosphere

(Jakosky et al., 2015). The science orbit of MAVEN has a 75° inclination. The periapsis altitude, the apoapsis altitude, and the orbital period are approximately 150 km, 6200 km, and 4.5 h, respectively.

The scientific instruments on board MAVEN enable the simultaneous measurements of ions, electrons, and the magnetic field. In this study, we use data obtained from the Solar Wind Electron Analyzer (SWEA) (Mitchell et al., 2016), the Suprathermal and Thermal Ion Composition (STATIC) analyzer (McFadden et al., 2015), the Solar Wind Ion Analyzer (SWIA) (Halekas et al., 2015), and the Magnetometer (MAG) (Connerney et al., 2015a).

SWEA is a symmetric hemispheric electrostatic analyzer with deflectors. It is designed to measure the energy and angular distributions of 5 eV to 4.6 keV electrons in the Martian environment with an energy resolution of $\Delta E/E = 17\%$. A field of view (FOV) is 360° × 120° (azimuth × elevation) for energies up to 1.6 keV. An angular resolution is 22.5° × 20° and a time resolution is 2 s. SWEA measures energy fluxes of electrons from 10^3 to 10^9 eV cm^{-2} s^{-1} sr^{-1} eV^{-1} (Mitchell et al., 2016). In this study, we used the SWEA measurements to identify the IMB crossing.

STATIC instrument uses a toroidal top-hat electrostatic analyzer (ESA) and a time-of-flight (TOF) velocity analyzer to resolve ion energy per charge, direction, and velocity per charge. It is designed to measure the ion mass compositions as well as the energy and angular distributions with time resolutions of 4–128 s. ESA has an energy range of 0.1 eV–30 keV to detect thermal ionospheric ions, suprathermal ion tails, and pick up ions with an energy resolution of $\Delta E/E = 15\%$. A FOV is 360° × 90° with an angular resolution of 22.5° × 6°. The TOF velocity analyzer resolves ion masses in the range of 1–70 atomic mass units (amu) with a mass resolution of 25%. STATIC measures energy fluxes of 10^4 to 10^8 eV cm^{-2} s^{-1} sr^{-1} eV^{-1} (McFadden et al., 2015). STATIC can produce 22 different data products, or Application Identifiers (APID) (McFadden et al., 2015). In this study, we mainly used the STATIC APID of the C6 mode (32 energy steps, 64 mass bins, and time resolution of 128 s) to identify the ICB crossing.

SWIA is a cylindrically symmetric electrostatic analyzer. It is designed to measure the properties of solar wind and magnetosheath ions (primarily protons), including their density, temperature, and velocity, in order to investigate the solar wind interactions with the Martian upper atmosphere. SWIA has an energy range of 25 eV–25 keV with an energy resolution of $\Delta E/E = 15\%$. A FOV is 360° × 90° with an angular resolution of 22.5°, and a time resolution of 4 s. In order to determine the solar wind proton and alpha particle angular distributions, SWIA uses a FOV of 3.75 ° × 4.5° with an angular resolution of 4.5°. SWIA measures an energy flux of 10^4 to 10^{11} eV cm^{-2} s^{-1} sr^{-1} eV^{-1} and determines the bulk plasma flow from solar wind speeds, and the solar wind density (Halekas et al., 2015). In this study, we used the SWIA measurements to identify the β^* boundary crossing and to obtain the solar wind parameters.

MAG consists of two independent triaxial fluxgate magnetometer sensors to measure the magnetic fields of the solar wind and the Martian upper atmosphere. MAG sensors are attached to the ends of each solar panel to minimize the relative contributions of the spacecraft-generated magnetic fields. The dynamic range of MAG is from 0.1 nT to 60,000 nT with a 32 vector samples per second time resolution, a 1° angular determination of the vector magnetic field, and a 5% precision of its scalar values (Connerney et al., 2015a, 2015b). In this study, we used the MAG measurements to identify the IMB and the β^* boundary crossing and to obtain the properties of IMF.

Since the periapsis of MAVEN changes with time, MAVEN is not always able to measure the upstream solar wind. During the periods of 27 November 2014 to 17 March 2015 and 4 June 2015 to 24 October 2015, the apoapsis of MAVEN was continuously in the upstream solar wind. In this study, we derived the upstream solar wind parameters, i.e., the solar wind velocity, density, and the magnetic field, as well as the solar wind dynamic pressure (P_{dyn}) from the SWIA and MAG observations. We used solar wind parameters in order to investigate the dependence of the plasma boundaries on the solar wind parameters.

We used the continuous simultaneous MAVEN datasets of ions, electrons, the magnetic field, and the solar wind parameters from November 2014 to March 2015 and June 2015 to October 2015.

3. Identification of Boundaries

3.1. Identification Method

In order to identify the IMB, ICB, and β^* boundary crossings, we developed an automated identification method based on the ion, electron, and magnetic field data from MAVEN. It should be noted that the data

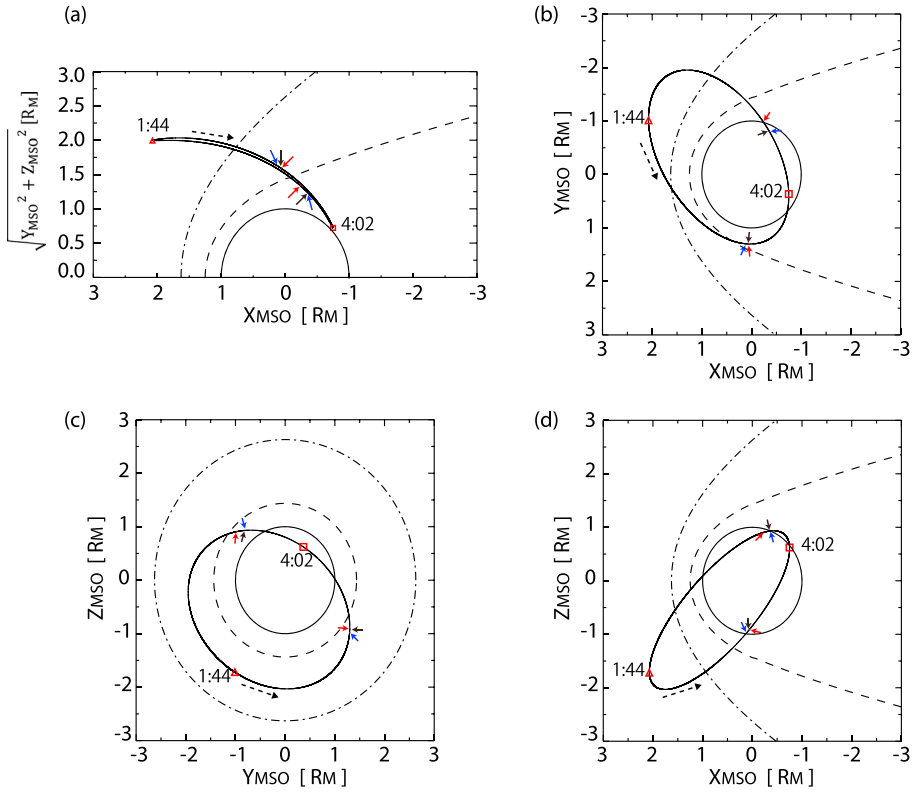


Figure 1. The MAVEN trajectories in the Mars-centered Solar Orbital (MSO) coordinates with units of Mars radii (R_M = 3397 km) for the 21 January 2015 event: Projections on (a) a cylindrical $X_{MSO} - \sqrt{Y_{MSO}^2 + Z_{MSO}^2}$, (b) $X_{MSO} - Y_{MSO}$, (c) $Y_{MSO} - Z_{MSO}$, (d) $X_{MSO} - Z_{MSO}$ planes are shown, respectively. Red, black, and blue arrows show the locations of the IMB, β^* boundary, and ICB crossings, respectively. The empirical models of the bow shock (BS) and the induced magnetosphere boundary (IMB) (Trotignon et al., 2006) are shown with the dash-dotted and dashed lines. The red square, red triangle, and black dotted arrow show the periapsis, the apoapsis, and the direction of the MAVEN orbit, respectively.

in the wake region, which is the sunshade region, are not used in this study. In this section, we describe the identification methods of each boundary.

As reported by many previous studies of either the IMB or MPB (e.g., Brain et al., 2003, 2006; Bertucci et al., 2005; Crider et al., 2005; Matsunaga et al., 2015; Nagy et al., 2004, and references therein; Trotignon et al., 2006), the IMB can be identified as the boundary where fluctuations of the magnetic field and the electron energy fluxes decrease from the magnetosheath value to that in the induced magnetosphere. On the dayside, increases in the magnetic field strength are also prominent across the IMB, while they are less clear on the nightside. Therefore, the identification of the IMB is based on the fluctuations of the magnetic field obtained from the MAG data and the electron fluxes from SWEA as follows.

First, the index of the magnetic field fluctuation (B_{index}) is calculated from the integrated power spectral density (PSD) above 0.1 Hz (PSD_B) using the wavelet analysis of the magnetic field fluctuation and the magnitude of the magnetic field (| $\boldsymbol{B}$ |):

$$B_{index} = PSD_B / | \boldsymbol{B} | \quad (1)$$

The use of PSD_B is similar to that employed in Matsunaga et al. (2015), and the normalization with | $\boldsymbol{B}$ | turned out to practical well identified the high magnetic field fluctuations in the magnetosheath. We eliminated the time intervals when B_{index} exceeded 0.5. We confirmed that this criterion can eliminate the magnetosheath time intervals by inspection.

After eliminating the magnetosheath region of the high B_{index}, the electron fluxes with energies of 80 eV are used to identify IMB. Namely, IMB is defined as the point when the time derivative of the 80 eV electron flux is the largest and the flux is greater than 2×10^6 cm^{-2} s^{-1} sr^{-1}. In order to avoid misselection by the electron flux

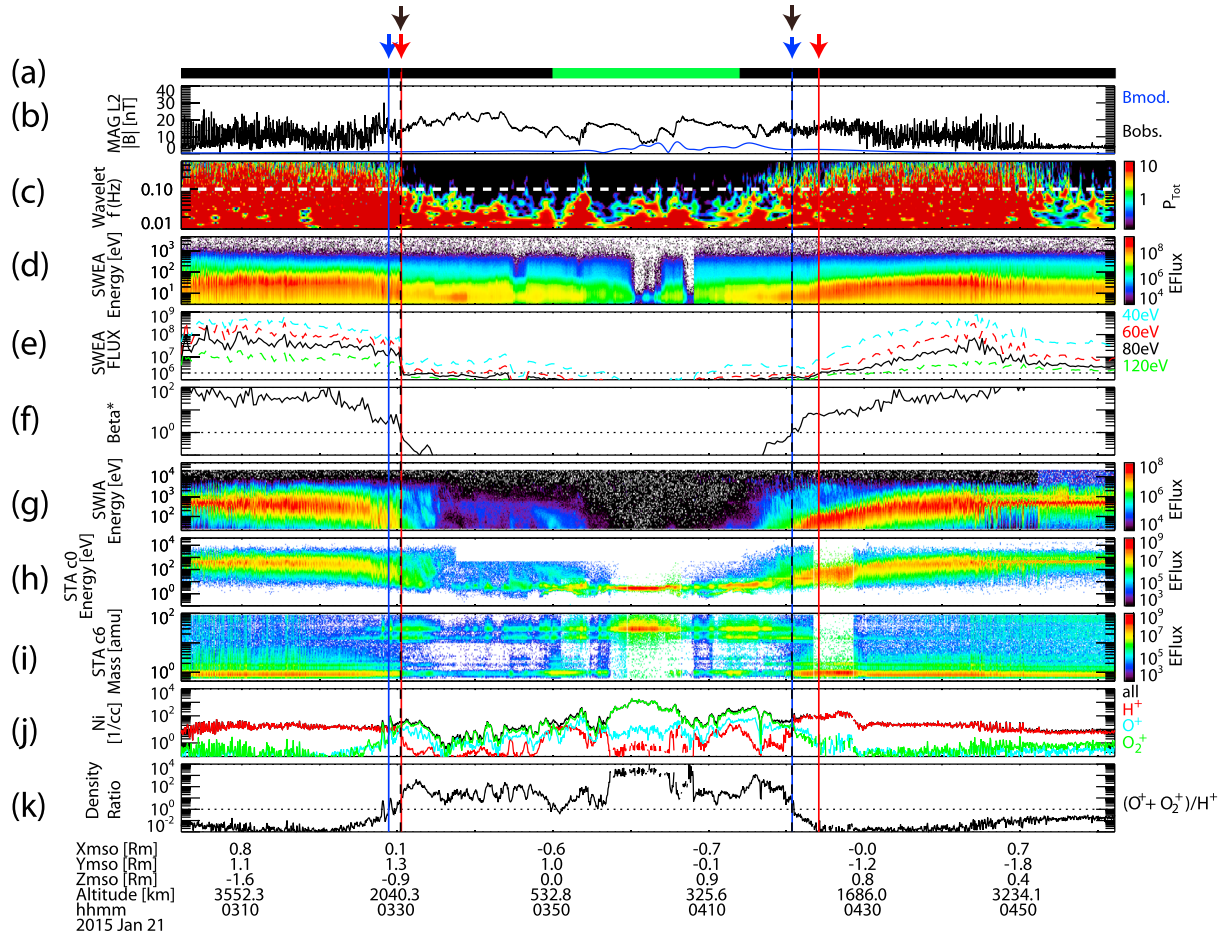


Figure 2. Time series plot of the plasma boundary crossing events observed by MAVEN on 21 January 2015: (a) the wake indices (black is not-wake regions), (b) the magnitude of the magnetic field (black line displaying the observations and the blue shows the crustal magnetic fields model (Cain et al., 2003)), (c) the wavelet spectrograph of the magnetic field data (white line is 0.1 Hz), (d) the electron energy flux, (e) the electron energy fluxes for the four energy ranges (horizontal dashed line is 2×10^6 cm^{-2} s^{-1} sr^{-1}), (f) the β^* value (horizontal dashed line is 1), (g) the ion energy flux from SWIA, (h) the ion energy flux from the STATIC C0 mode, (i) the ion mass flux from the STATIC C6 mode, (j) ion number densities from STATIC, and (k) the ion number density ratio r_i (horizontal dashed line is 1). The red and blue vertical lines and arrows indicate the time indices of the IMB and ICB crossings, respectively. The black vertical dashed lines and arrows indicate the time indices of the β^* boundary crossings. The periapsis is at 04:02:13.

fluctuations in the ionosphere, the lower limit of the electron flux was set. According to the MEX observations (Dubinin et al., 2006) and MGS observations (Trotignon et al., 2006), the electron flux of 80 eV is dominant in the magnetosheath region and characteristically changes after crossing the IMB. The spacecraft potential was corrected in the data used. Finally, the obtained IMB crossing was examined by inspection, and the misidentified events were eliminated. Using both the magnetic field and electron criteria described above, 1097 IMB crossings were identified in 1294 orbits of MAVEN. It should be noted that we carried out a similar analysis with an electron flux of 40 eV, which confirmed that the statistical results reported in this study do not change.

As for the ICB crossings, previous studies (e.g., Breus et al., 1991; Dubinin et al., 2006; Lundin et al., 1989; Sauer et al., 1994) showed that the ion composition often changes drastically from predominantly solar wind protons (H^+) to predominantly planetary heavy ions (O^+, O_2^+) as the satellite approaches the planet. Therefore, we use the ion number density ratio r_i from STATIC in order to identify the ICB crossings, where r_i is defined as

$$r_i = (n_{O^+} + n_{O_2^+})/n_{H^+} \quad (2)$$

Namely, the timing of $r_i = 1$ at the position closest to the planet was chosen as the ICB crossing. Thus, $r_i \geqq 1$ is satisfied inside the ICB. The calculation of the density was carried out after correcting for the spacecraft potential and the straggling issue of STATIC. Since the ion number density ratio shows fluctuations, we exclude the short enhancement events with duration less than 20 s. After the identification of the ICB crossings, the

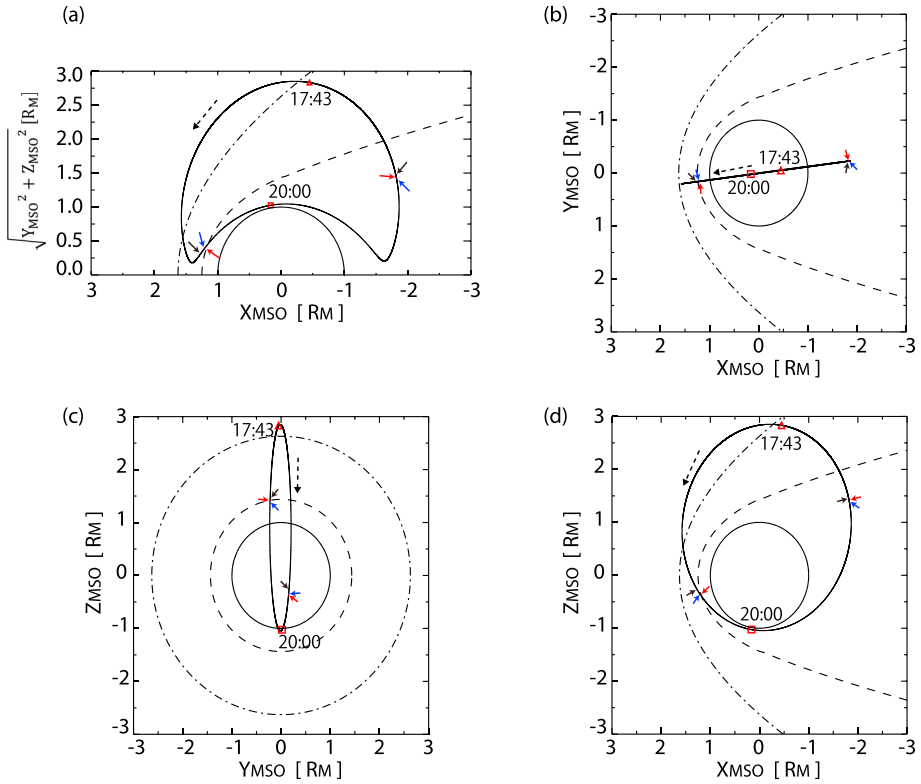


Figure 3. The MAVEN trajectories in the MSO coordinates for the 16 September 2015 event. The format is the same as in Figure 1.

validity of the crossing was verified by inspection and vague events were eliminated. As a result, we obtained 1709 ICB crossings in 1294 orbits of MAVEN.

In this study, we adopted the β^* value in order to identify the location of the pressure balance boundary:

$$\beta^* \equiv (P_{\mathrm{th}} + P_{\mathrm{dyn}})/P_B = 1 \tag{3}$$

where P_{th}, P_{dyn}, and P_B indicate the thermal, dynamic, and magnetic pressures, respectively. For the calculations of the former two values, the ion number density, velocity, and temperature obtained from SWIA are used. After the identification of the time of the β^* boundary crossings, the validity of the crossing was verified by inspection; we identified 1107 β^* boundary crossings in 1294 orbits of MAVEN. Since SWIA does not discriminate between ion species, SWIA moments are computed under the assumption that all ions are protons. SWIA also cannot measure cold ions with energies below 25 eV. Therefore, when a significant number of heavy ions exist, there is a possibility of pressure overestimation. On the other hand, the existence of undetected cold ions can cause a pressure underestimation. We checked the ion number density ratio r_i described above, which is calculated from STATIC at the identified of β^* boundary locations and found that the median of r_i for all β^* boundary crossings is 0.04. Thus, we think the effects of the heavy ions on the SWIA moments do not qualitatively change the results of this study.

3.2. Examples of the Boundary Identification

Based on the identification method of plasma boundaries described in the previous subsection, we show two typical examples of MAVEN observations of plasma boundary crossings on 21 January 2015 and 16 September 2015. As shown in Figure 1a, both the inbound (trajectory toward periapsis) and outbound (trajectory away from periapsis) passes of the orbit traverse the empirical IMB (dashed line) around terminator in the event on 21 January 2015. The boundary crossings are shown by arrows in each panel of Figure 1; the crossing during the inbound pass occurs in the southern hemisphere, while the outbound pass occurs in the northern hemisphere.

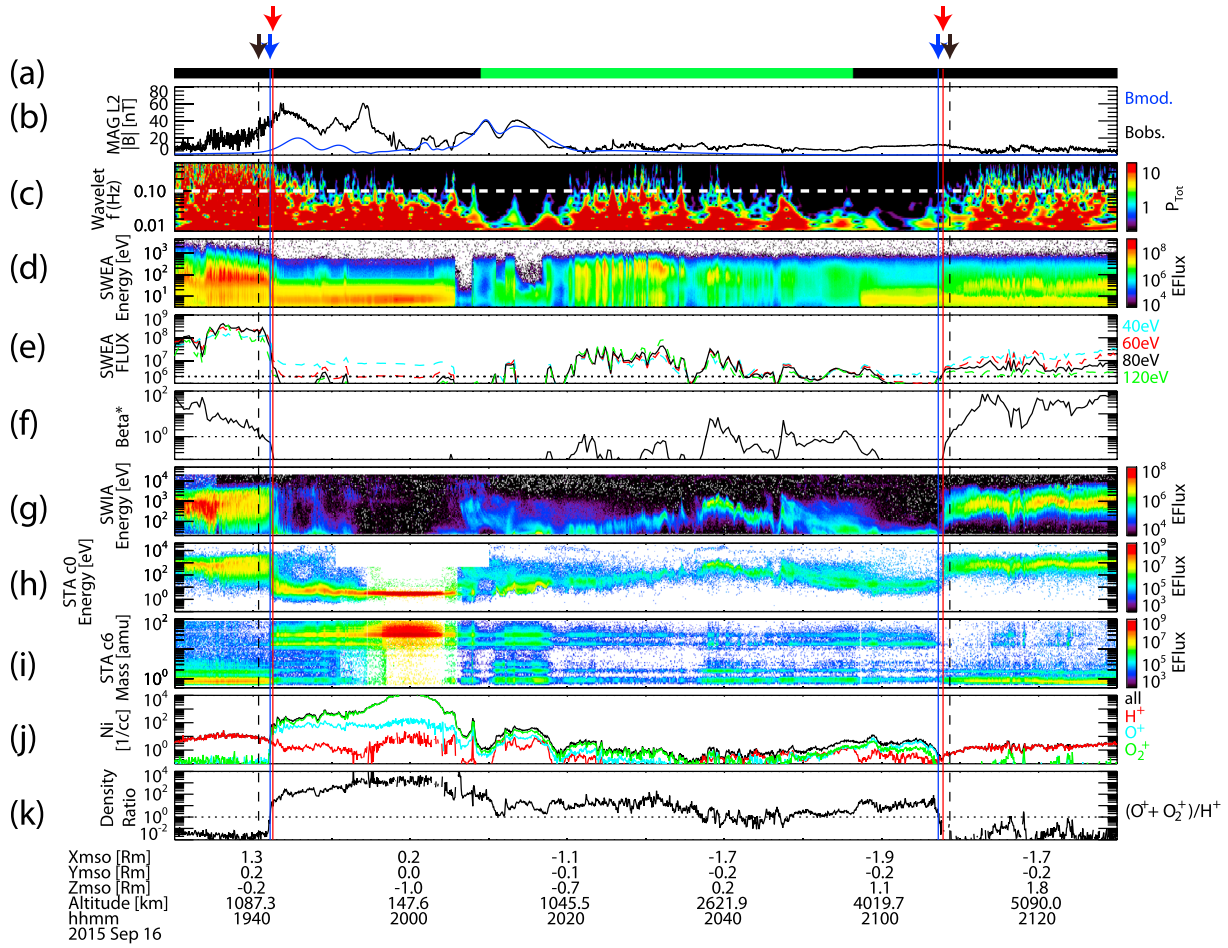


Figure 4. Time series plot of the plasma boundary crossing events observed by MAVEN on 16 September 2015. The red and blue vertical lines and arrows indicate the time indices of the IMB, and ICB crossings, respectively. The black vertical dashed lines and arrows indicate the time indices of the β^* boundary crossings. The format is the same as in Figure 2. The periapsis is at 20:00:21.

For the inbound boundary crossings around the terminator in the southern hemisphere, the location of the ICB (left blue line in Figure 2) is higher than those of the other boundaries. The location of the IMB (left red line in Figure 2) is similar to that of the β^* boundary (left black dashed line in Figure 2). In the outbound crossings around the terminator in the northern hemisphere, the location of the IMB (right red line in Figure 2) is higher than those of the other two boundaries. The location of the ICB (right blue line in Figure 2) is similar to that of the β^* boundary (right black line in Figure 2). The P_{dyn} of the inbound and outbound passes on 21 January 2015 are 0.9 nPa and 1.4 nPa, respectively.

During the event on 16 September 2015, the inbound boundary crossings were observed on the dayside of the southern hemisphere, while the outbound crossings occurred on the nightside of the northern hemisphere (Figure 3). In the inbound crossings, the location of the ICB (left blue line in Figure 4) is similar to that of the IMB (left red line in Figure 4). The location of the β^* boundary (left black dashed line in Figure 4) is higher than those of the other two boundaries. In the outbound crossings, the location of the IMB (right red line in Figure 4) is higher than that of the ICB (right blue line in Figure 4). The location of the β^* boundary (right black dashed line in Figure 4) is higher than those of the other two boundaries. The P_{dyn} of the inbound and outbound passes on 16 September 2015 are 1.4 nPa and 0.8 nPa. These examples suggest that the relative locations of the IMB, ICB, and β^* boundary can change with the hemispheres and/or the solar zenith angle (SZA).

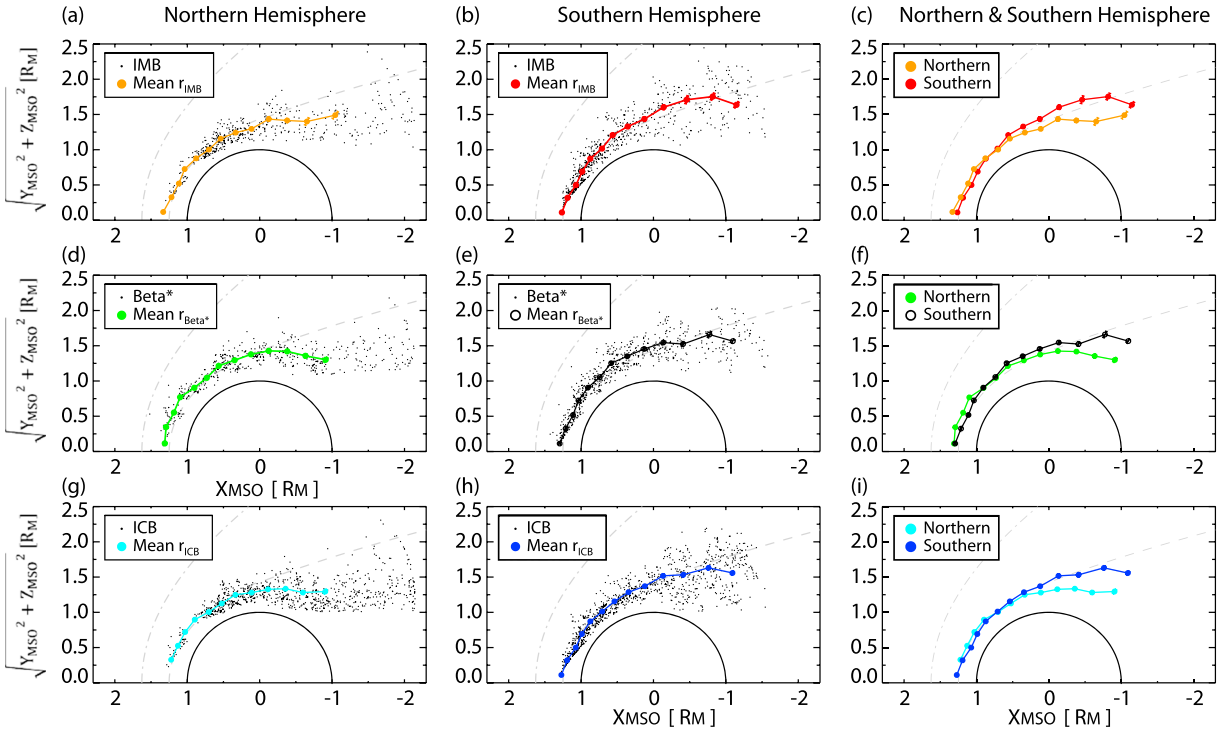


Figure 5. The observed locations of the (a–c) IMB, (d–f) β^* boundary, and (g–i) ICB in cylindrical coordinates (left is sunward). Figures 5a, 5d, and 5g, 5b, 5e, and 5h, and 5c, 5f, and 5i show the crossing events in the northern hemisphere, the southern hemisphere, and both hemispheres, respectively. The mean altitudes at every 10° of SZA were plotted in all panels. Since the number of events where SZA $\geqq$ 140° in the southern hemisphere is small, the mean value of the distance in the radial direction was calculated for SZA $\leqq$ 130°. The empirical models of the BS and the IMB (Trotignon et al., 2006) are shown with the gray dash-dotted and dashed lines. Error bars show the standard error.

4. Statistical Properties

4.1. Average Boundary Locations in Cylindrical Coordinates

As mentioned in sections 2 and 3, approximately 8 months of data were used for the statistical study except for the data in the wake region. We conducted statistical analyses of the locations of the three plasma boundaries (IMB, ICB, and β^* boundary) crossings, which are identified using the methods described in section 3.1. The identified boundary locations are plotted in cylindrical coordinates in Figure 5. The figures also show the mean value of the radial distance ($r = \sqrt{X_{MSO}^2 + Y_{MSO}^2 + Z_{MSO}^2}$) for every 10° of SZA as circles with the standard error as an error bar. When we compared the boundary locations between the geographic northern (Figures 5a, 5d, and 5g) and southern hemispheres (Figures 5b, 5e, and 5h), all boundaries tend to be located at higher altitudes in the southern hemisphere than in the northern hemisphere on the nightside (SZA > 90°). This north-south asymmetry is in Figures 5c, 5f, and 5i, which show only the mean distance in each hemisphere, and is consistent with the simulation results (Ma et al., 2002).

Compare the relative locations including the IMB (red), β^* boundary (black), and ICB (blue) shown in Figure 6, we can see that the IMB and the ICB almost coincide on the dayside (SZA $\leqq$ 90°). This feature can be seen both in the northern (Figure 6a) and southern (Figure 6b) hemispheres. The β^* boundary tend to be located higher than the other boundaries on the dayside.

Next, we investigated the effect of the solar wind dynamic pressure (P_{dyn}) on the three plasma boundaries. As shown in each panel of Figure 7, all the boundaries have the same dependence on the P_{dyn} regardless of the geographical hemisphere: during the high P_{dyn} period (red and orange in Figure 7), the boundaries tend to be located at lower altitudes than those during the low P_{dyn} period (green and blue). These results indicate that the locations of all the boundaries are affected by the P_{dyn}, and they are consistent with previous studies (e.g., Brain et al., 2003, 2006; Matsunaga et al., 2015).

The clear geographic north-south asymmetry shown in Figure 6 directed us to investigate the effect of the Martian crustal magnetic fields on the three plasma boundaries. Since MAVEN is a single spacecraft, it is

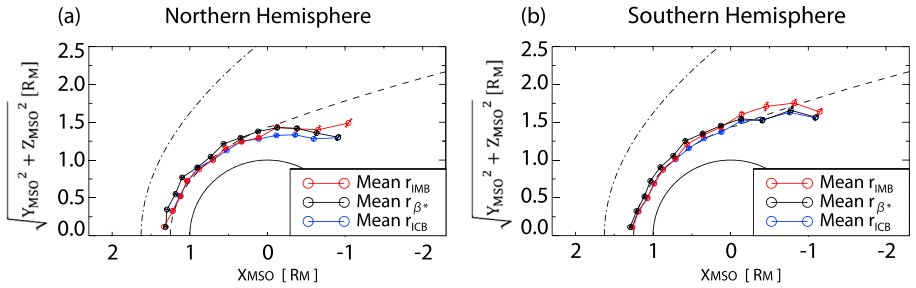


Figure 6. The mean altitude for every 10° of SZA: The red, black, and blue circles show the IMB, β^* boundary, and ICB, respectively. (a and b) Events in the northern and the southern hemisphere, respectively. The axis format is the same as in Figure 5.

difficult to quantitatively evaluate the effects of crustal magnetic fields when MAVEN crosses each of the boundaries. In order to investigate the locations and qualitative effects of the strong crustal magnetic fields, we used the east longitude above the subsolar point (hereafter, this east longitude is referred to as "subsolar ELON") at the time of each crossing event. From the MGS observation of the crustal magnetic fields, the strong crustal magnetic fields region ranges over 150°–210° east longitude (Connerney et al., 2005). The dependence on the subsolar ELON is shown in Figure 8. The different colors in each panel in Figure 8 correspond to different subsolar ELON.

In the northern hemisphere (Figures 8a, 8c, and 8e), it is difficult to recognize any variation related to the subsolar ELON. On the other hand, in the southern hemisphere (Figures 8b, 8d, and 8f), the mean altitudes of all the boundaries are higher when the crustal magnetic fields are dayside (magenta and orange in Figure 8) than they are at any other times. Note when the subsolar ELON is 90°–150°, all the boundaries are located

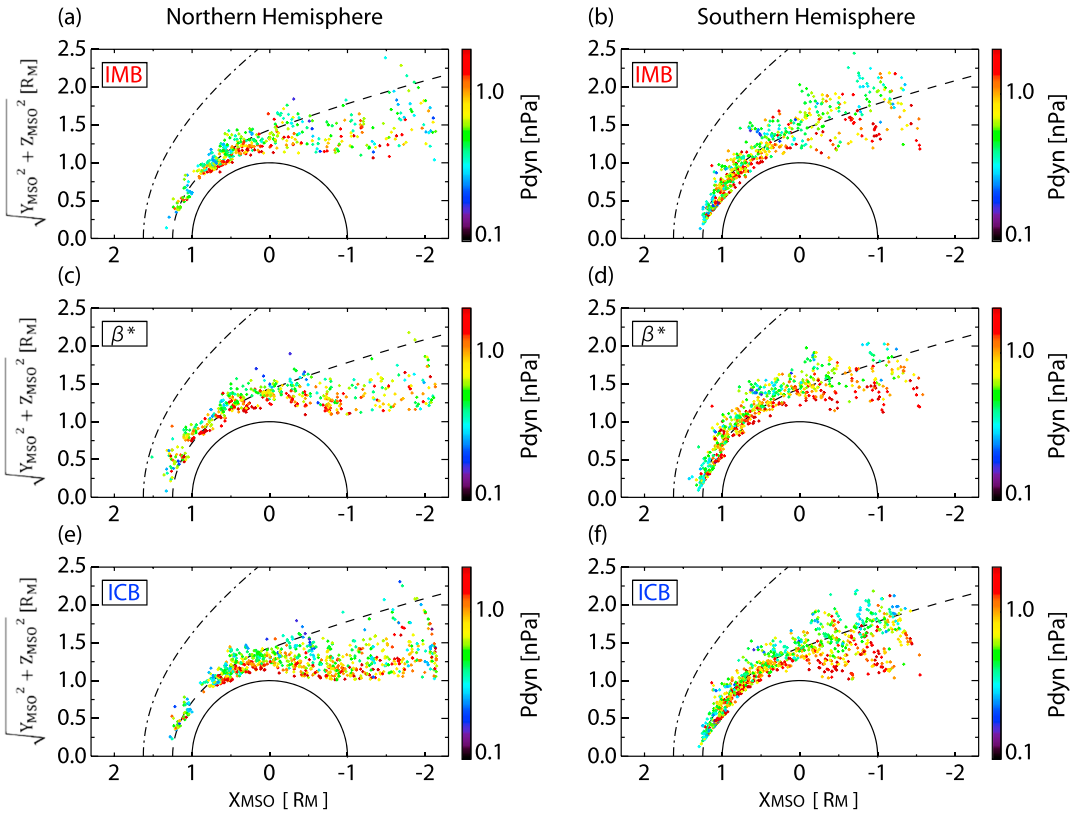


Figure 7. The observational locations of the (a and b) IMB, (c and d) β^* boundary, and (e and f) ICB. Figures 7a, 7c, and 7e and 7b, 7d, 7f use only events in the northern and the southern hemispheres, respectively. The color code shows the solar wind dynamic pressures. The axis format is the same as in Figure 5.

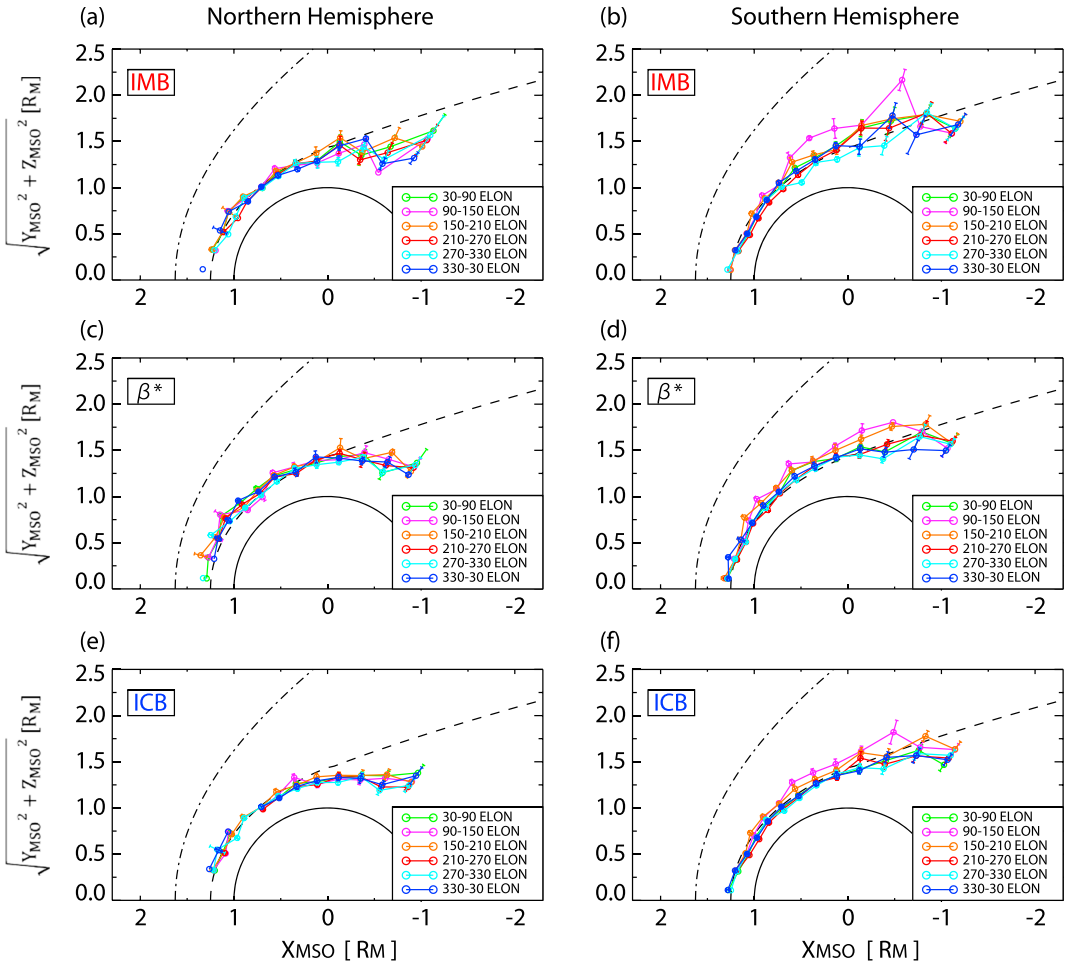


Figure 8. The mean altitude of the (a and b) IMB, (c and d) β^* boundary, (e and f) and ICB. These values are calculated at every 10° of SZA and every 60° of the east longitude above the subsolar point. The axis format is the same as in Figure 5.

the highest altitude. These results show that all the boundaries tend to be located at high altitudes when the strong crustal magnetic fields region is on the dayside. However, it should be noted that on the nightside of the southern hemisphere, all the boundaries tend to be located at higher altitudes than those in the northern hemisphere regardless of the crustal magnetic fields locations.

4.2. Relative Distances Between IMB, ICB, and β^* Boundary

In this section, we investigate the relative distances between the IMB, ICB, and β^* boundary using the crossings of each boundary identified during the same orbit. Figure 9 shows the relations between the radial distances of the ICB, r_{ICB}, and the relative distances between the IMB and ICB (d$r = r_{ICB} - r_{IMB}$, red dots), and between the β^* boundary and ICB (d$r = r_{ICB} - r_{\beta^*}$, black dots) as well as their mean value (red and black square) for every 0.1 R_M of r_{ICB}. In Figure 9, $r_{ICB} - r_{IMB} > 0$ denotes that the ICB is located outside of the IMB, while $r_{ICB} - r_{IMB} < 0$ denotes that the ICB is located inside of the IMB. On the dayside (Figures 9a and 9c), the IMB and ICB tend to be located at similar positions in both hemispheres, and the β^* boundary tends to be located outside of the other boundaries. On the nightside, the IMB tends to be located outside of the ICB in both hemispheres. However, the scattering of the data is large and there are occasions when the ICB is located outside of the IMB on the nightside. The β^* boundary tends to be located outside of the ICB. When the ICB is located at high altitudes, the β^* boundary tends to be located at a similar or lower position than the ICB.

In order to further investigate the reason for the large scattering on the nightside, here we investigated the relationship between the relative distances of the ICB and IMB on the nightside and the solar wind convection electric field. To investigate the effect of the solar wind convection electric field, we used the latitude of the MAVEN spacecraft expressed in the Mars-Sun-Electric field (MSE) coordinate system. The MSE coordinate

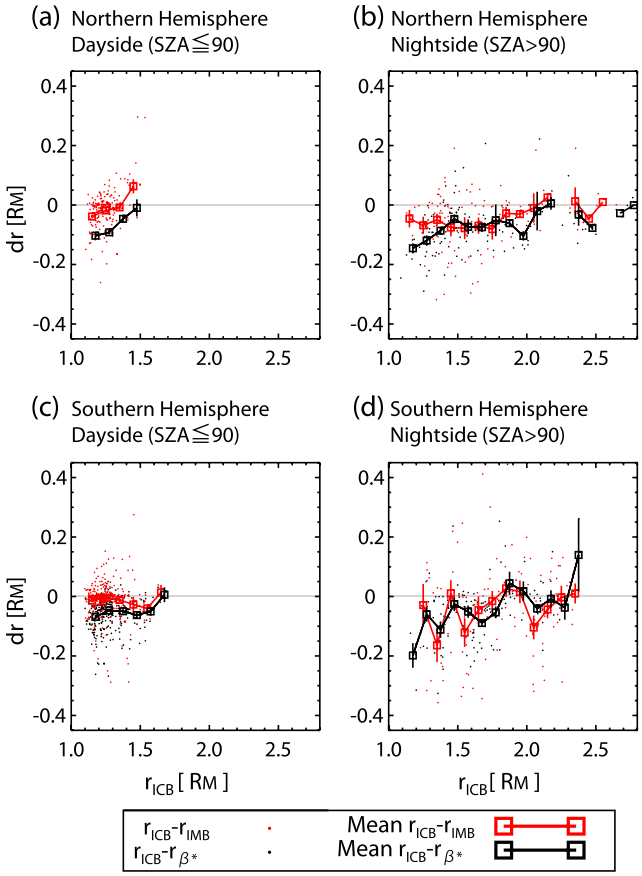


Figure 9. Red and black dots show the relative distances between the IMB and the ICB and between the β^* boundary and the ICB, respectively. The squares show each mean value at every 0.1 R_M of r_{ICB}. R_M denotes Mars radii (3397 km). (a and b, and c and d) The northern and the southern hemispheres, respectively. Figures 9a and 9c, and 9b and 9d show the results for on the dayside and nightside, respectively. The gray solid line shows the relative distance of 0.

system is defined as follows: the X_{MSE} axis points from Mars to the Sun, the Z_{MSE} axis points along the direction of the solar wind convection electric field, $\boldsymbol{E}_{SW} = -\boldsymbol{V}_{SW} \times \boldsymbol{B}$ (IMF in the solar wind region $\boldsymbol{B}$ is measured by MAG and the solar wind velocity $\boldsymbol{V}_{SW}$ is from the SWIA data), and the Y_{MSE} axis completes the right-handed system. Then, the MSE latitude (θ_{MSE}) is computed via $\arctan(Z_{MSE}/\sqrt{X_{MSE}^2 + Y_{MSE}^2})$. We assume that the upward E_{SW} hemisphere is in $\theta_{MSE} \geqq 30°$, and the downward E_{SW} hemisphere is in $\theta_{MSE} \leqq -30°$ and exclude events near the equator.

We also exclude the effects of time variations of the solar wind. We set two criteria to select the time periods of steady solar wind conditions. The solar wind parameters were calculated for each orbit from the average values of the direct solar wind observations near the MAVEN apoapsis. One criterion is that the difference in the IMF clock angle obtained from MAG observed just before and after the boundary crossings is less than 30°. The other one is that the difference in the P_{dyn} values obtained from SWIA before and after the crossings is ±30%. Through these selection criteria, we obtained the 203 ICB and IMB crossing events on the nightside under the steady solar wind conditions.

As shown in Figures 10a and 10c, the IMB is located at a similar distance or is outside of the ICB in the nightside northern hemisphere regardless of the E_{SW} direction as well as the crustal magnetic fields. In the nightside southern hemisphere (Figures 10b and 10d), there are more high r_{ICB} events ($r_{ICB} > 2.0\ R_M$) in the downward E_{SW} hemisphere (Figure 10d) than in the upward E_{SW} hemisphere (Figure 10b). If we focus on the high r_{ICB} events shown in the right-hand side of Figure 10d, there are some points of $dr > 0$. These positive dr points have magenta and orange, which correspond to the presence of strong crustal magnetic fields on the dayside. Namely, when the strong crustal magnetic fields region is on the dayside, the ICB tends to be located outside of the IMB in the downward E_{SW} hemisphere. Under these specific conditions, the mean values of relative

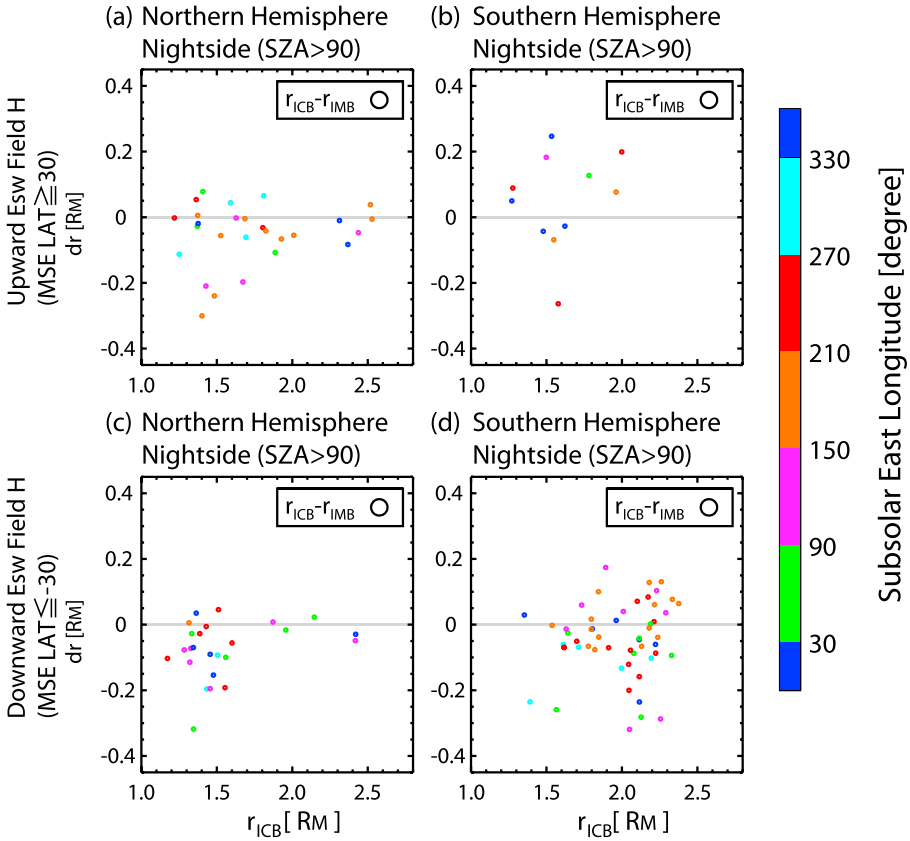


Figure 10. Circles show the relative distances between the IMB and ICB on the nightside colored by the east longitude above the subsolar point. (a and b, and c and d) The results for the upward ($\theta_{MSE} \geqq 30°$) and downward solar wind convection electric field ($\theta_{MSE} \leqq -30°$) hemispheres, respectively. Figures 10a and 10c, and 10b and 10d show the results for the northern and southern hemispheres, respectively. The gray solid line shows the relative distance of 0.

distances between the ICB and IMB crossing events are 0.08 R_M ~272 km, and the mean values of the radial distance of ICB crossing events are 2.11 R_M ~7200 km.

5. Summary and Discussion

In this study, we reported the results of a statistical investigation of the Martian plasma boundaries: the induced magnetosphere boundary (IMB), the ion composition boundary (ICB), and the pressure balance boundary based on β^*. In order to understand the differences and/or similarities between the IMB, ICB, and β^* boundary and their dependences on the solar wind, this study used ion, electron, and magnetic field data observed by MAVEN. We used the data from the time period 27 November 2014 to 17 March 2015 and from 4 June 2015 to 24 October 2015, when the direct solar wind observations of each orbit are available.

We developed a method for automatically identifying the IMB, ICB, and β^* boundary crossings and identified 1097 IMB crossing events, 1709 ICB crossing events, and 1107 β^* boundary crossing events over the 1294 orbits of MAVEN.

All the boundaries show an asymmetry between the geographic northern and southern hemispheres (Figures 5c, 5f, and 5i). The locations of all the boundaries are affected by P_{dyn} as well as by the crustal magnetic fields. During a high P_{dyn} period, all the boundaries tend to be located at lower altitudes than usual. The effect of crustal magnetic fields causes all the boundaries to be located at higher altitudes. These results are consistent with previous observations (e.g., Brain et al., 2003, 2006; Fang et al., 2017; Matsunaga et al., 2015). However, mainly on the nightside, all the boundaries tend to locate at higher altitudes in the southern hemisphere than in the northern hemisphere regardless of the crustal magnetic field locations. This pattern indicates that the crustal magnetic fields seem to have a permanent effect that raises the boundary altitude on the nightside. In fact, the results of the MHD model from Luhmann et al. (2015) show

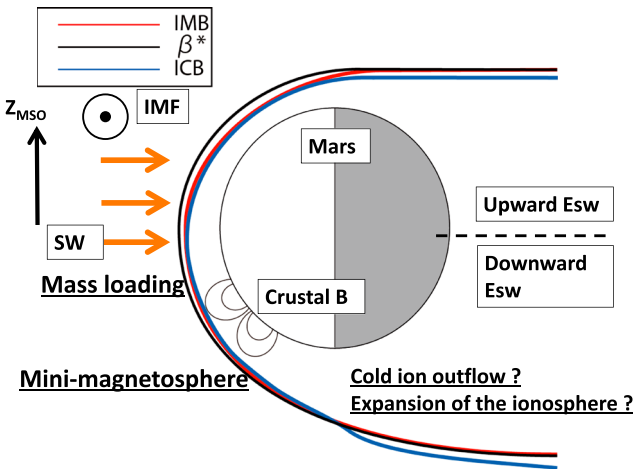


Figure 11. A summary sketch of the Martian plasma boundaries. The IMB, ICB, and β^* boundaries are the red, blue, and black solid lines, respectively. SW denotes the solar wind. The $+Z_{MSO}$ direction corresponds to the direction of the northern hemisphere. The direction of the IMF makes the northern hemisphere correspond to the hemisphere of the upward convection electric field.

that the induced magnetosphere can spread to higher altitudes in the southern hemisphere in the tail region, regardless of the local times of strong crustal magnetic fields.

The IMB and ICB tend to be located at similar positions on the dayside. On the other hand, the IMB tends to be located at higher altitudes than the ICB on the nightside. These results suggest that the mass loading process (e.g., Trotignon et al., 2001) is the dominant influence in forming the IMB and the ICB on the dayside. On the nightside, based on previous studies, the transition region has a mantle structure (e.g., Dubinin et al., 1996). It is assumed that the outside of the mantle is the IMB, and it seems that the density of solar wind protons gradually decreases via expansion waves in the mantle region (e.g., Siscoe et al., 2001). Thus, the density balance points (ICB) between the solar wind protons (H^+) and the planetary heavy ions (O^+, O_2^+) are naturally below the IMB.

The β^* boundary tends to be located at higher altitudes than the other boundaries on the dayside. Since we used 80 eV electron fluxes to identify the IMB, high-energy electron fluxes may contribute to the plasma pressure in the magnetosheath, leading the IMB lower than the β^* boundary. The MHD simulation also showed that the β^* boundary tends to be located higher than the ICB (Xu et al., 2016).

The IMB and ICB tend to be located at higher altitudes than usual in the nightside southern hemisphere, where the E_{SW} is downward (toward the planet). The mean value and the standard deviation of r_{ICB} in the nightside upward E_{SW} hemisphere are 1.60 R_M and 0.24 R_M, respectively. On the other hand, those in the nightside downward E_{SW} hemisphere are 1.98 R_M and 0.26 R_M, respectively. IMB crossings are located above the ICB on average; however, the ICB is tends to be located above the IMB in the downward E_{SW} with the r_{ICB} higher than 2.0 R_M. The 3-D hybrid and multi-ion species simulations (Modolo et al., 2005) and the MEX observations (Dubinin et al., 2012) suggest the expansion of the ionosphere in the downward E_{SW} hemisphere. The expansion of the ionosphere may push the ICB up to high altitude.

Our results show that the combined effect of the crustal magnetic fields and the downward E_{SW} can raise the location of the ICB to be higher than the IMB on the nightside. Since there is no significant variation of the number density of H^+ in the high r_{ICB} events, the high location of ICB is likely caused by heavy ions denser than usual at high altitudes. At high altitudes, the number density of pickup heavy ions is insufficient to significantly change the ICB locations. Hence, a candidate physical mechanism might be the enhanced cold ion outflow in the mini-magnetospheres (Lundin et al., 2011) via processes such as the cold ion outflow from the cusps (Lundin et al., 2006) or the magnetic reconnection between the crustal magnetic fields and IMF (e.g., Hara et al., 2017). The dayside open crustal magnetic fields can reconnect with the IMF, allowing dense cold heavy ions to escape from the cusp region of the mini-magnetospheres. Note that there is no clear evidence that the cold ion outflow from the mini-magnetospheres is more enhanced in the downward E_{SW} hemisphere rather than in the upward E_{SW} hemisphere. As for asymmetry of the upward and downward E_{SW} hemispheres, less acceleration (smaller velocity) in the downward E_{SW} than in the upward E_{SW} hemisphere on the course of upward transport of outflowing ions might be a cause of denser heavy ions at high altitudes ($r_{ICB} > 2.0\ R_M$), which resulting in higher ICB location than IMB even at high altitudes. However, the characteristic of the cold ion outflow is out of scope of this paper.

6. Conclusion

Based on statistical analyses of the MAVEN data, we obtained the following results concerning the three plasma boundaries: the induced magnetosphere boundary (IMB), the ion composition boundary (ICB), and the pressure balance boundary based on β^* (see the summary sketch in Figure 11):

1. On the dayside (SZA $\leqq 90°$), the IMB and the ICB tend to be located at similar positions. This concurrence suggests that the mass loading process is dominant in forming both the IMB and the ICB. The β^* boundary tend to be located higher than other boundaries.

2. On the nightside (SZA > 90°), the locations of all the boundaries are higher in the geographic southern hemisphere than in the northern hemisphere. This pattern suggests that the crustal magnetic fields seem to have permanent effects in raising the boundary altitudes.
3. The solar wind dynamic pressure affects the locations of all boundaries. During the high dynamic pressure period, all the boundaries tend to be located at low altitudes.
4. From investigation of individual events, the IMB is located outside of the ICB on average. However, the locations of the ICB tend to be higher than usual and outside of the IMB in the downward E_{SW} hemisphere, when the strong crustal fields are located on the dayside. It indicates that the dense heavy ions should be distributed higher than usual, presumably owing to is the enhancement of the cold ion outflow from the mini-magnetospheres and/or the expansion ionosphere.

Acknowledgments
This work was supported by Grant-in-Aid for Scientific Research (a) 16H02229 and (b) 15H03731 by Japan Society for the Promotion of Science (JSPS). Kazunari Matsunaga was supported by a research fellowship of Nagoya University Program for Leading Graduate Schools of "Leadership Development Program for Space Exploration and Research" from JSPS. The MAVEN project is supported by NASA Mars Exploration Program. The MAVEN data are available in NASA Planetary Data System. We are grateful to all MAVEN mission members.

References

Acuña, M. H., Connerney, J. E. P., Wasilewski, P., Lin, R. P., Anderson, K. A., Carlson, C. W., … Ness, N. F. (1998). Magnetic field and plasma observations at Mars: Initial results of the Mars Global Surveyor mission. *Science*, *279*, 1676–1680. https://doi.org/10.1126/science.279.5357.1676

Albee, A. L., Arvidson, R. E., Palluconi, F., & Thorpe, T. (2001). Overview of the Mars Global Surveyor mission. *Journal of Geophysical Research*, *106*(E12), 23,291–23,316. https://doi.org/10.1029/2000JE001306

Bertucci, C., Mazelle, C., AcuñA, M. H., Russell, C. T., & Slavin, J. A. (2005). Structure of the magnetic pileup boundary at Mars and Venus. *Journal of Geophysical Research*, *110*, A01209. https://doi.org/10.1029/2004JA010592

Brain, D., Barabash, S., Boesswetter, A., Bougher, S., Brecht, S., Chanteur, G., … Terada, N. (2010). A comparison of global models for the solar wind interaction with Mars. *Icarus*, *206*, 139–151. https://doi.org/10.1016/j.icarus.2009.06.030

Brain, D. A., Bagenal, F., Acuña, M. H., & Connerney, J. E. P. (2003). Martian magnetic morphology: Contributions from the solar wind and crust. *Journal of Geophysical Research*, *108*(A12), 1424. https://doi.org/10.1029/2002JA009482

Brain, D. A., Halekas, J. S., Lillis, R., Mitchell, D. L., Lin, R. P., & Crider, D. H. (2005). Variability of the altitude of the Martian sheath. *Geophysical Research Letters*, *32*, L18203. https://doi.org/10.1029/2005GL023126

Brain, D. A., Mitchell, D. L., & Halekas, J. S. (2006). The magnetic field draping direction at Mars from April 1999 through August 2004. *Icarus*, *182*, 464–473. https://doi.org/10.1016/j.icarus.2005.09.023

Breus, T. K., Bauer, S. J., Krymskii, A. M., & Mitnitskii, V. Y. (1989). Mass loading in the solar wind interaction with Venus and Mars. *Journal of Geophysical Research*, *94*, 2375–2382. https://doi.org/10.1029/ JA094iA03p02375

Breus, T. K., Dubinin, E. M., Krymskii, A. M., Lundin, R., Luhmann, J. G., Yeroshenko, Y. G., … Styashkin, V. A. (1991). The solar wind interaction with Mars: Consideration of Phobos 2 mission observations of an ion composition boundary on the dayside. *Journal of Geophysical Research*, *96*, 11165Ű11174. https://doi.org/10.1029/91JA01131

Cain, J. C., Ferguson, B. B., & Mozzoni, D. (2003). An $n = 90$ internal potential function of the Martian crustal magnetic field. *Journal of Geophysical Research*, *108*, 5008. https://doi.org/10.1029/2000JE001487

Connerney, J. E. P., Acuña, M. H., Ness, N. F., Kletetschka, G., Mitchell, D. L., Lin, R. P., & Rème, H. (2005). Tectonic implications of Mars crustal magnetism. *Proceedings of the National Academy of Sciences*, *102*, 14,970–14,975. https://doi.org/10.1073/pnas.0507469102

Connerney, J. E. P., Espley, J., Lawton, P., Murphy, S., Odom, J., Oliversen, R., & Sheppard, D. (2015a). The MAVEN magnetic field investigation. *Space Science Reviews*, *195*, 257–291. https://doi.org/10.1007/s11214-015-0169-4

Connerney, J. E. P., Espley, J. R., DiBraccio, G. A., Gruesbeck, J. R., Oliversen, R. J., Mitchell, D. L., … Jakosky, B. M. (2015b). First results of the MAVEN magnetic field investigation. *Geophysical Research Letters*, *42*, 8819–8827. https://doi.org/10.1002/2015GL065366

Crider, D. H., Espley, J., Brain, D. A., Mitchell, D. L., Connerney, J. E. P., & Acuña, M. H. (2005). Mars Global Surveyor observations of the Halloween 2003 solar superstorm's encounter with Mars. *Journal of Geophysical Research*, *110*, A09S21. https://doi.org/10.1029/2004JA010881

Dubinin, E., & Lundin, R. (1995). Mass-loading near Mars. *Advances in Space Research*, *16*, 75–79. https://doi.org/10.1016/0273-1177(95)00211-V

Dubinin, E., Fränz, M., Woch, J., Roussos, E., Barabash, S., Lundin, R., … Acuña, M. (2006). Plasma morphology at Mars. Aspera-3 Observations. *Space Science Reviews*, *126*, 209–238. https://doi.org/10.1007/s11214-006-9039-4

Dubinin, E., Fraenz, M., Woch, J., Modolo, R., Chanteur, G., Duru, F., … Lundin, R. (2012). Upper ionosphere of Mars is not axially symmetrical. *Earth, Planets, and Space*, *64*, 113–120. https://doi.org/10.5047/eps.2011.05.022

Dubinin, E. M., Sauer, K., Lundin, R., Baumgärtel, K., & Bogdanov, A. (1996). Structuring of the transition region (plasma mantle) of the Martian magnetosphere. *Geophysical Research Letters*, *23*, 785–788. https://doi.org/10.1029/96GL00701

Fang, X., Ma, Y., Masunaga, K., Dong, Y., Brain, D., Halekas, J., … Dong, C. (2017). The Mars crustal magnetic field control of plasma boundary locations and atmospheric loss: MHD prediction and comparison with MAVEN. *Journal of Geophysical Research: Space Physics*, *122*, 4117–4137. https://doi.org/10.1002/2016JA023509

Gurnett, D. A., Morgan, D. D., Duru, F., Akalin, F., Winningham, J. D., Frahm, R. A., … Barabash, S. (2010). Large density fluctuations in the Martian ionosphere as observed by the Mars Express radar sounder. *Icarus*, *206*, 83–94. https://doi.org/10.1016/j.icarus.2009.02.019

Halekas, J. S., Taylor, E. R., Dalton, G., Johnson, G., Curtis, D. W., McFadden, J. P., … Jakosky, B. M. (2015). The solar wind ion analyzer for MAVEN. *Space Science Reviews*, *195*, 125–151. https://doi.org/10.1007/s11214-013-0029-z

Hara, T., Brain, D. A., Mitchell, D. L., Luhmann, J. G., Seki, K., Hasegawa, H., … Jakosky, B. M. (2017). MAVEN observations of a giant ionospheric flux rope near Mars resulting from interaction between the crustal and interplanetary draped magnetic fields. *Journal of Geophysical Research: Space Physics*, *122*, 828–842. https://doi.org/10.1002/2016JA023347

Jakosky, B. M., Lin, R. P., Grebowsky, J. M., Luhmann, J. G., Mitchell, D. F., Beutelschies, G., … Zurek, R. (2015). The Mars Atmosphere and Volatile Evolution (MAVEN) mission. *Space Science Reviews*, *195*, 3–48. https://doi.org/10.1007/s11214-015-0139-x

Luhmann, J. G., Dong, C., Ma, Y., Curry, S. M., Mitchell, D., Espley, J., … Mazelle, C. (2015). Implications of MAVEN Mars near-wake measurements and models. *Geophysical Research Letters*, *42*, 9087–9094. https://doi.org/10.1002/2015GL066122

Lundin, R., Zakharov, A., Pellinen, R., Borg, H., Hultqvist, B., Pissarenko, N., … Koskinen, H. (1989). First measurements of the ionospheric plasma escape from Mars. *Nature*, *341*, 609–612. https://doi.org/10.1038/341609a0

Lundin, R., Winningham, D., Barabash, S., Frahm, R., Holmström, M., Sauvaud, J.-A., … Wurz, P. (2006). Plasma acceleration above Martian magnetic anomalies. *Science*, *311*, 980–983. https://doi.org/10.1126/science.1122071

Lundin, R., Barabash, S., Dubinin, E., Winningham, D., & Yamauchi, M. (2011). Low-altitude acceleration of ionospheric ions at Mars. *Geophysical Research Letters*, *38*, L08108. https://doi.org/10.1029/2011GL047064

Ma, Y., Nagy, A. F., Hansen, K. C., Dezeeuw, D. L., Gombosi, T. I., & Powell, K. G. (2002). Three-dimensional multispecies MHD studies of the solar wind interaction with Mars in the presence of crustal fields. *Journal of Geophysical Research*, *107*, 1282. https://doi.org/10.1029/2002JA009293

Matsunaga, K., Seki, K., Hara, T., & Brain, D. A. (2015). Asymmetric penetration of shocked solar wind down to 400 km altitudes at Mars. *Journal of Geophysical Research: Space Physics*, *120*, 6874–6883. https://doi.org/10.1002/2014JA020757

McFadden, J. P., Kortmann, O., Curtis, D., Dalton, G., Johnson, G., Abiad, R., … Jakosky, B. (2015). MAVEN SupraThermal and Thermal Ion Compostion (STATIC) instrument. *Space Science Reviews*, *195*, 199–256. https://doi.org/10.1007/s11214-015-0175-6

Mitchell, D. L., Lin, R. P., Mazelle, C., Rème, H., Cloutier, P. A., Connerney, J. E. P., … Ness, N. F. (2001). Probing Mars' crustal magnetic field and ionosphere with the MGS electron reflectometer. *Journal of Geophysical Research*, *106*(E10), 23,419–23,428. https://doi.org/10.1029/2000JE001435

Mitchell, D. L., Mazelle, C., Sauvaud, J.-A., Thocaven, J.-J., Rouzaud, J., Fedorov, A., … Jakosky, B. M. (2016). The MAVEN solar wind electron analyzer. *Space Science Reviews*, *200*, 495–528. https://doi.org/10.1007/s11214-015-0232-1

Modolo, R., Chanteur, G. M., Dubinin, E., & Matthews, A. P. (2005). Influence of the solar EUV flux on the Martian plasma environment. *Annales Geophysicae*, *23*, 433–444. https://doi.org/10.5194/angeo-23-433-2005

Nagy, A. F., Gombosi, T. I., Szego, K., Sagdeev, R. Z., Shapiro, V. D., & Shevchenko, V. I. (1990). Venus mantle-Mars planetosphere—What are the similarities and differences?. *Geophysical Research Letters*, *17*, 865–868. https://doi.org/10.1029/GL017i006p00865

Nagy, A. F., Winterhalter, D., Sauer, K., Cravens, T. E., Brecht, S., Mazelle, C., … Trotignon, J. G. (2004). The plasma environment of Mars. *Space Science Reviews*, *111*, 33–114. https://doi.org/10.1023/B: SPAC.0000032718.47512.92

Riedler, W., Schwingenschuh, K., Moehlmann, D., Oraevskii, V. N., Eroshenko, E., & Slavin, J. (1989). Magnetic fields near Mars—First results. *Nature*, *341*, 604–607. https://doi.org/10.1038/341604a0

Ruhunusiri, S., Halekas, J. S., McFadden, J. P., Connerney, J. E. P., Espley, J. R., Harada, Y., … Hasegawa, H. (2016). MAVEN observations of partially developed Kelvin-Helmholtz vortices at Mars. *Geophysical Research Letters*, *43*, 4763–4773. https://doi.org/10.1002/2016GL068926

Sauer, K., Bogdanov, A., & Baumgärtel, K. (1994). Evidence of an ion composition boundary (protonopause) in bi-ion fluid simulations of solar wind mass loading. *Geophysical Research Letters*, *21*, 2255–2258. https://doi.org/10.1029/94GL01691

Siscoe, G. L., Erickson, G. M., Sonnerup, B. U. Ö, Maynard, N. C, Siebert, K. D., Weimer, D. R., & White, W. W. (2001). Relation between cusp and mantle in MHD simulation. *Journal of Geophysical Research*, *106*, 10,743–10,750. https://doi.org/10.1029/2000JA000385

Trotignon, J. G., Dubinin, E., Grard, R., Barabash, S., & Lundin, R. (1996). Martian planetopause as seen by the plasma wave system onboard Phobos 2. *Journal of Geophysical Research*, *101*, 24,965–24,978. https://doi.org/10.1029/96JA01898

Trotignon, J. G., Séran, H.-C., Béghin, C., Meyer-Vernet, N., Manning, R., Grard, R., & Laakso, H. (2001). In situ observations of the ionized environment of Mars: The antenna impedance measurements experiment, AIM, proposed as part of the Mars advanced radar for subsurface and ionospheric sounding, MARSIS. *Planetary and Space Science*, *49*, 155–164. https://doi.org/10.1016/S0032-0633(00)00134-3

Trotignon, J. G., Mazelle, C., Bertucci, C., & Acuña, M. H. (2006). Martian shock and magnetic pile-up boundary positions and shapes determined from the Phobos 2 and Mars Global Surveyor data sets. *Planetary and Space Science*, *54*, 357–369. https://doi.org/10.1016/j.pss.2006.01.003

Vignes, D., Mazelle, C., Rme, H., Acuña, M. H., Connerney, J. E. P., Lin, R. P., … Ness, N. F. (2000). The solar wind interaction with Mars: Locations and shapes of the bow shock and the magnetic pile-up boundary from the observations of the MAG/ER experiment onboard Mars Global Surveyor. *Geophysical Research Letters*, *27*(1), 49–52. https://doi.org/10.1029/1999GL010703

Xu, S., Liemohn, M. W., Dong, C., Mitchell, D. L., Bougher, S. W., & Ma, Y. (2016). Pressure and ion composition boundaries at Mars. *Journal of Geophysical Research: Space Physics*, *121*, 6417–6429. https://doi.org/10.1002/2016JA022644